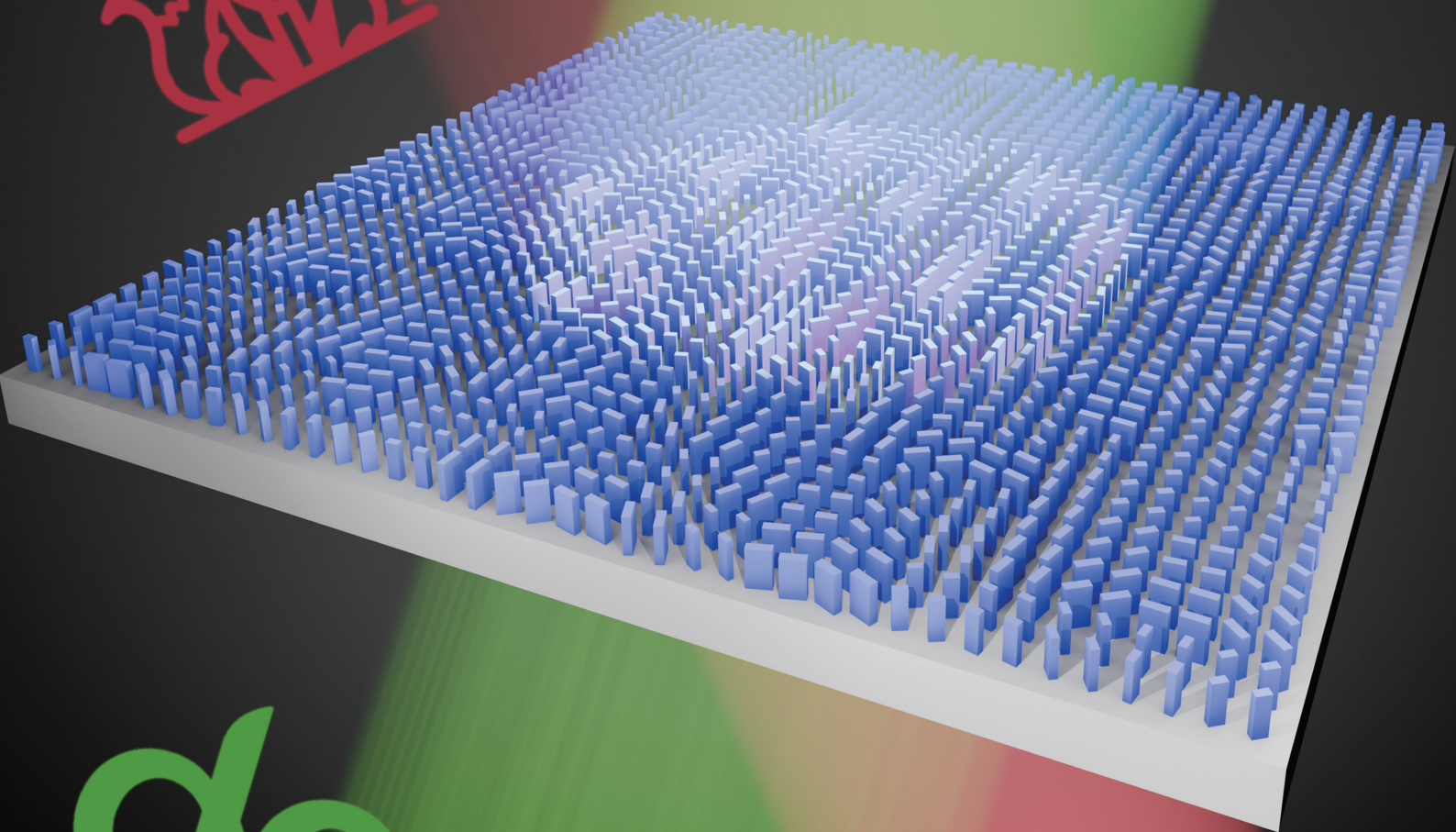


# ADVANCED OPTICAL MATERIALS



# Directionally Asymmetric Holographic Imaging for Arbitrary Polarization States Using Janus Metasurfaces

Yu-Chuan Chang, Chang-Yi Lin, Huan-Teng Su, Yun-Chien Wu, Chih-Yao Hsu, Shu-Ming Chang, and Yao-Wei Huang\*

Janus metasurfaces have emerged as a powerful platform for directionally asymmetric holographic imaging. However, existing designs often suffer from limitations such as complex fabrication processes, reliance on spatial multiplexing or vertical stacking, restricted polarization control, or significant Ohmic losses—particularly preventing operation in the visible spectrum. In this study, single-layer dielectric Janus metasurface holograms are presented utilizing TiO<sub>2</sub> meta-atoms, each capable of operating simultaneously for forward and backward illumination, to overcome these obstacles. By incorporating the Dammann grating principle and precise phase manipulation, this design generates high-fidelity holographic images for arbitrary polarized light at wavelength of 532 nm. This approach not only achieves simplified fabrication and minimizes losses but also broadens the applicability of holography, paving the way for diverse innovations in compact and versatile optical technologies.

capabilities—such as lenses,<sup>[10,11]</sup> holograms,<sup>[10–12]</sup> and dual frequency control.<sup>[13,14]</sup> However, most of these studies rely on metallic antennas operating in the microwave regime.<sup>[10,12,14]</sup> Although plasmonic Janus metasurfaces using gold and magnesium antennas have been realized for hydrogen- and oxygen-responsive tuning in the visible range, these systems suffer significant losses.<sup>[15]</sup> Moreover, metallic antennas typically function at only one polarization, necessitating spatial multiplexing strategies to encode different directional responses into separate polarization states or subpixels—a method that reduces effective cross-section and lowers efficiency. To address these drawbacks, Si-based Janus metasurfaces with enhanced functionalities have been demonstrated.<sup>[16,17]</sup>

## 1. Introduction

The term “Janus” originates from the two-faced Roman god who looked simultaneously to the past and the future, symbolizing the capability to exhibit different characteristics when viewed from opposite directions. This directional asymmetry has been harnessed in nanophotonics to realize a variety of functionalities,<sup>[1]</sup> including Janus metamaterials,<sup>[2,3]</sup> Janus photonic crystals,<sup>[4–6]</sup> and non-reciprocal devices.<sup>[7–9]</sup> As interest grows in controlling light on a subwavelength scale at a single interface, Janus metasurfaces have naturally emerged. Existing research on Janus metasurfaces demonstrates impressive

However, these approaches require a two-layer (vertically stacked) configuration and remain limited to the mid-infrared and near-infrared regimes. Other studies incorporate materials such as graphene or vanadium dioxide for tunability,<sup>[18,19]</sup> or employ nonlinear materials for nonreciprocal transmission,<sup>[20,21]</sup> yet these methods often demand multiple vertically stacked layers. Moreover, both the spatial multiplexing and vertical stacking strategies discussed above support only linear or circular polarization states. In contrast, our previous work introduced a single-layer, TiO<sub>2</sub>-based Janus metasurface enabling arbitrary polarization states in the visible range.<sup>[22]</sup> However, realizing directionally asymmetric holographic image generation—an essential milestone for near-field to far-field photonic control—in a purely single-layer design without spatial multiplexing has yet to be demonstrated.

In this letter, we present single-layer Janus metasurface holograms capable of reconstructing different images under forward and backward illumination, as illustrated in **Figure 1**. We employ a Jones matrix approach, combined with propagation and geometric phase control in rectangular nanopillars, enabling operation at arbitrary polarization states—including not only linear and circular, but also elliptical polarizations. In practice, we showcase two types of Janus metasurface holograms. In **Figure 1a**, Sample 1 targets left-circularly polarized (LCP) illumination, reconstructing “nycu” (an abbreviation of National Yang Ming Chiao Tung University) under forward incidence and a fox (the NYCU mascot) under backward incidence. In **Figure 1b**, Sample 2 is optimized for elliptical polarization, yielding “dp”

Y.-C. Chang, C.-Y. Lin, H.-T. Su, Y.-C. Wu, C.-Y. Hsu, S.-M. Chang, Y.-W. Huang  
Department of Photonics  
College of Electrical and Computer Engineering  
National Yang Ming Chiao Tung University  
Hsinchu 300093, Taiwan  
E-mail: ywh@nycu.edu.tw

The ORCID identification number(s) for the author(s) of this article can be found under <https://doi.org/10.1002/adom.202501546>

© 2025 The Author(s). Advanced Optical Materials published by Wiley-VCH GmbH. This is an open access article under the terms of the [Creative Commons Attribution](#) License, which permits use, distribution and reproduction in any medium, provided the original work is properly cited.

DOI: 10.1002/adom.202501546

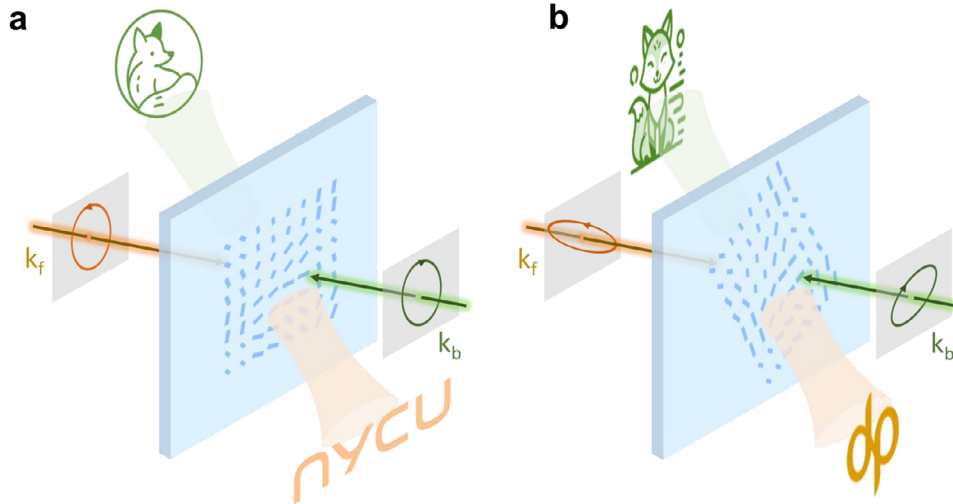


**Figure 1.** Schematics of our Janus metasurface holograms. a) Design optimized for circular polarization. b) Design optimized for elliptical polarization.  $k_f$  and  $k_b$  represent the directions in which polarized light propagates forward and backward respectively.

(representing the Department of Photonics) in forward incidence and another fox in backward incidence. Both metasurfaces are fabricated as a single layer of  $\text{TiO}_2$  nanopillars, deposited on a glass substrate, with precisely tailored widths and rotation angles to operate at visible wavelengths. This research establishes a versatile design principle for directionally asymmetric multifunctionality, paving the way for broader applications in compact optical components, including advanced imaging, beam shaping, and other holographic technologies, not only in the visible band but across a wider range of wavelengths.<sup>p</sup>

## 2. Results

### 2.1. Local and Global Matrix of Janus Metasurface Holograms

Janus metasurfaces derive their functionality from a global Jones matrix, which in turn is governed by the local Jones matrices of individual meta-atoms. In designing Janus metasurface holograms, our primary goal is to optimize these meta-atoms, the fundamental building blocks of the metasurface. This optimization involves adjusting their arrangement, shape, size, and rotation angle so that arbitrarily polarized light, incident from forward and backward directions, produces the desired holographic images. In our implementation, we employ rectangular nanopillar structures as meta-atoms, which perform similarly to birefringent linear waveplates. Their properties can be expressed mathematically as:

$$J = R(-\alpha) \begin{bmatrix} e^{i\varphi_x} & 0 \\ 0 & e^{i\varphi_y} \end{bmatrix} R(\alpha) \quad (1)$$

$$J' = R(-\alpha') \begin{bmatrix} e^{i\varphi_x} & 0 \\ 0 & e^{i\varphi_y} \end{bmatrix} R(\alpha') \quad (2)$$

In this notation, the prime symbol (') denotes the backward coordinate system.<sup>[22]</sup> The parameters  $\varphi_x$  and  $\varphi_y$  represent the phase delays for the local  $x$ - and  $y$ -components of the

incident field ( $E_x$  and  $E_y$ ), respectively, while  $R(\alpha)$  is the rotation matrix describing the rotation of each meta-atom by an angle  $\alpha$ .

To create a unified coordinate framework for our design, we account for the interplay between the forward and backward coordinates, leading to the global Jones matrix of the Janus metasurface holograms:<sup>[22]</sup>

$$J(x, y) = \begin{bmatrix} (e^{i\varphi_f(x,y)} + e^{i\varphi_b(x,y)}) \cos \chi \sin \chi & e^{-i\delta} (e^{i\varphi_f(x,y)} - e^{i\varphi_b(x,y)}) \cos^2 \chi \\ e^{-i\delta} (e^{i\varphi_f(x,y)} - e^{i\varphi_b(x,y)}) \sin^2 \chi & e^{-i2\delta} (e^{i\varphi_f(x,y)} + e^{i\varphi_b(x,y)}) \cos \chi \sin \chi \end{bmatrix} \quad (3)$$

Here,  $\delta$  denotes the phase difference between global  $E_x$  and  $E_y$ , while  $\chi$  is defined by  $\tan^{-1}(E_y/E_x)$ . This corresponds to the incident polarized state  $|\lambda(\chi, \delta)\rangle = [\cos \chi; e^{i\delta} \sin \chi]$ . The terms  $\varphi_f$  and  $\varphi_b$  correspond to the phase distributions of the desired holographic images for forward and backward incidence, respectively. These phase profiles are obtained using the Gerchberg-Saxton algorithm within the framework of computer-generated holography (CGH).<sup>[23,24]</sup>

A comparison between the global and local matrices reveals a physical constraint that requires the off-diagonal elements of Equation (3) to be identical.<sup>[25]</sup> This condition restricts  $\chi$  for the incident light on Janus metasurface holograms to be  $\pi/4$ , corresponding to  $\pm 45^\circ$  linearly polarized, circularly polarized, and certain specific elliptically polarized states, thereby significantly limiting the range of possible polarized states.

To circumvent this restriction, we introduce a rotation angle  $\beta$  to the global matrix, transforming it into  $J_\beta$ . The resulting transformation can be expressed as:

$$J|\lambda(\pi/4, \delta)\rangle = JR(-\beta)R(\beta)|\lambda\rangle = J_\beta|\lambda(\chi_d, \delta_d)\rangle \quad (4)$$

where  $|\lambda(\chi_d, \delta_d)\rangle$  describes the incident polarized state with arbitrary  $\chi_d$  and  $\delta_d$ . The rotation angle  $\beta$  is linked to the angle of polarization  $\gamma(\chi, \delta) = \frac{1}{2} \tan^{-1}(\tan 2\chi \cos \delta)$ . Accordingly,  $\beta = \gamma(\chi,$

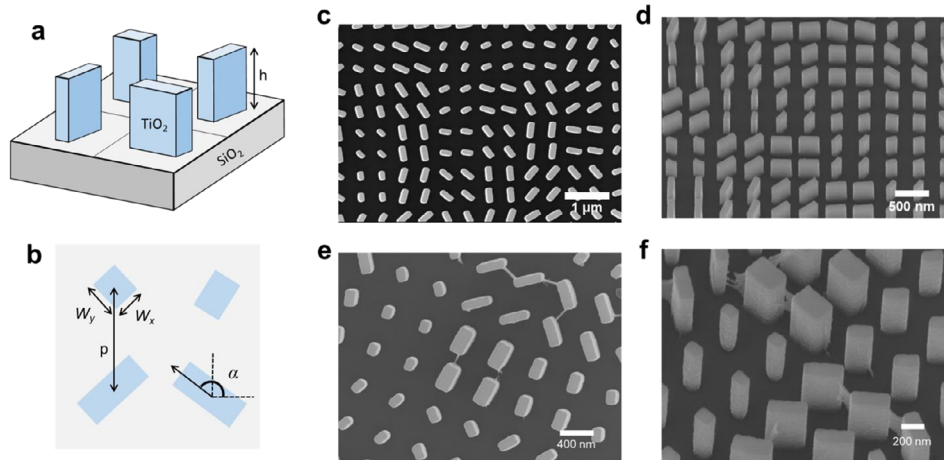


**Figure 2.** Design and fabricated Janus metasurface holograms. a,b) Schematic of  $\text{TiO}_2$ -based rectangular meta-atoms arranged on the glass substrate in a square lattice with fixed height,  $h = 600$  nm, and period,  $p = 480$  nm. The widths and rotation angle of meta-atoms are denoted as  $W_x$ ,  $W_y$ , and  $\alpha$ . c,d) The scanning electron microscope (SEM) images of part of Janus metasurface hologram for polarization state with  $\chi = \pi/4$  and  $\delta = \pi/2$ . e,f) The SEM images of part of Janus metasurface hologram for polarization state with  $\chi = \pi/6$  and  $\delta = \pi/3$ . The images on the left are from top-view, and those on the right are from side-view. The SEM images from side-view are obtained with a tilted angle 30 degree.

$\delta) - \gamma(\pi/4, \delta)$ , where  $\gamma(\pi/4, \delta)$  corresponds to the original constraint  $\chi = \pi/4$  imposed by Janus metasurface holograms.

In practice, to demonstrate arbitrary polarization capability, we present two types of Janus metasurface holograms operating under left-circularly polarized and elliptically polarized light. Mathematically, these polarization states can be expressed as  $|\pi/4, \pi/2\rangle$  and  $|\pi/6, \pi/3\rangle$ , respectively. The first state lies outside the  $\chi$  constraint, whereas the second one is constrained, necessitating a global rotation of the latter sample. The required rotation angle is  $\beta = \gamma(\pi/6, \pi/3) - \pi/4 \approx -24.55^\circ$ . Detailed information on both samples, including their operating polarization states and ideal reconstructed images, is provided in **Table 1**.

**Table 1.** Two Janus metasurface holograms and their desired polarization states and images.

	$ \lambda(\chi, \delta)\rangle$	Forward image	Backward image
Sample 1	$ \frac{\pi}{4}, \frac{\pi}{2}\rangle$		
Sample 2	$ \frac{\pi}{6}, \frac{\pi}{3}\rangle$		

## 2.2. Design and Fabrication

We chose rectangular,  $\text{TiO}_2$ -based meta-atoms with a height ( $h$ ) of 600 nm and a base period ( $p$ ) of 480 nm, arranged in a square lattice on a fused silica, as illustrated in **Figure 2a,b**. By combining the theory of propagation and geometric phase, we tailored the widths ( $W_x$ ,  $W_y$ ) and rotation angle ( $\alpha$ ) of each meta-atom to achieve the desired phase delay and wave retardation, while also maintaining high transmittance at a wavelength of 532 nm, based on a phase-to-width lookup table (**Figure S1**, Supporting Information). The resulting metasurface hologram comprise  $550 \times 550$  pixels, each constructed from arrays of these meta-atoms.

To ensure reliable measurement results, each pixel of the Janus metasurface holograms contains 4 identical meta-atoms, effectively increasing the pixel size to  $2p = 0.96 \mu\text{m}$ , and this configuration yields single-layout holograms of  $528 \mu\text{m} \times 528 \mu\text{m}$ , as depicted in **Figure 3a**. The zero-order diffractive image range, i.e., the overall field of view (FOV), in the far field along the  $x$ - or  $y$ -direction is governed by the pixel size and is calculated to be  $\pm 16.1^\circ$  via  $\pm \sin^{-1}[\lambda/(4p)]$ , leading to a total angular range of  $\approx 32.2^\circ$  (**Figure 3b**). The actual usable FOV, however, also depends on the spatial extent of the ideal designed image. For example, the “nycu” forward image of Sample 1 spans  $\approx 19.84^\circ$  in FOV (details provided in **Figure S2**, Supporting Information). Consequently, while the pixel size determines the FOV, the total size of the Janus metasurface hologram in the near field dictates the angular resolution in the far field (i.e., the angular size of each far-field pixel).

In holographic imaging, fidelity refers to how accurately a reconstructed image reproduces its intended target. Achieving high fidelity is crucial for preserving fine details and minimizing distortions. However, a major factor that degrades fidelity in holography is speckle noise, which arises from high coherence of laser illumination. Speckle appears as a granular interference pattern that diminishes the clarity and uniformity of the reconstructed

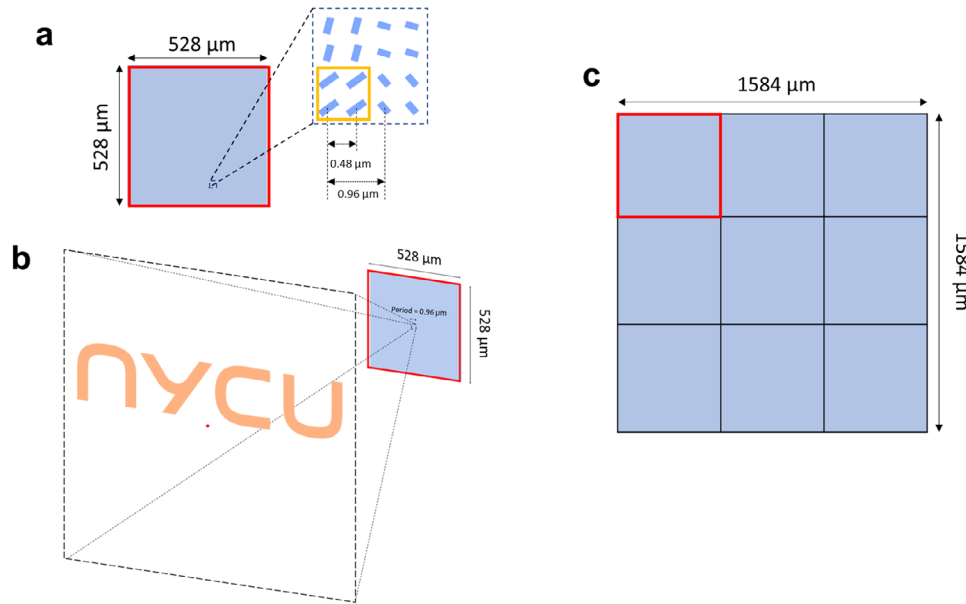


**Figure 3.** Schematics of Janus metasurface holograms based on the concept of Dammann grating. a) Single layout of Janus metasurface hologram in size of  $528 \mu\text{m} \times 528 \mu\text{m}$  with four identical meta-atoms arranged in a pixel (yellow box). b) Schematic of forward holographic imaging by Janus metasurface hologram. The diffraction angle of the image is decided by a pixel (yellow box), while the resolution is controlled by the size of Janus metasurface hologram. The red spot is used to simulate the zero-order diffraction. c) Illustration of Janus metasurface hologram composed of 3-by-3 same single layout as shown in (a) to generate holographic images with high fidelity.

image. A promising strategy for both enhancing fidelity and suppressing speckle involves the use of Dammann gratings.<sup>[23]</sup> In our approach, these metasurface holograms generate multiple uniform diffraction beams, thereby improving the overall uniformity of the holographic reconstructions.

The theoretical derivation is as follows. Let the near-field distribution of the designed hologram be  $u(x, y) = e^{i\phi(x,y)}$ , and let its corresponding far-field distribution  $U(k_x, k_y)$  be obtained via CGH. To incorporate Dammann gratings into the hologram design, we periodically tile this near-field distribution in two dimensions. In practice, the modified near-field distribution  $u'(x, y)$  is expressed as

$$u'(x, y) = u(x, y) \otimes \left[ \text{comb}\left(\frac{x}{W}, \frac{y}{W}\right) \text{rect}\left(\frac{x}{NW}\right) \text{rect}\left(\frac{y}{NW}\right) \right] \quad (5)$$

where  $W$  represents the spatial extent of  $u(x, y)$  ( $528 \mu\text{m}$ ), and  $N$  denotes the number of periodic tilings in an  $N \times N$  arrangement. Consequently, the modified far-field distribution  $U'(k_x, k_y)$  can be written as

$$U'(k_x, k_y) \propto U(k_x, k_y) \times \left\{ \text{comb}(Wk_x, Wk_y) \otimes [\text{sinc}(NWk_x) \text{sinc}(NWk_y)] \right\} \quad (6)$$

Here, we choose  $N = 3$ , resulting in a sample size of  $1584 \mu\text{m} \times 1584 \mu\text{m}$ , as illustrated in Figure 3c. The new holographic image ( $|U'(k_x, k_y)|^2$ ) resembles the original holographic image ( $|U(k_x, k_y)|^2$ ) multiplied by a dot array, where each adjacent dot is separated by 3 pixels in the  $k$ -space. With this design, we enhance the fidelity of holographic images while mitigating speckle noise.

Our fabrication process follows a precise sequence. First, we spin-coat a layer of electron beam resist (ZEP 520A, Zeon) onto

the fused glass substrate to achieve a uniform thickness of  $600 \text{ nm}$ . Next, we spin-coat a thin polymer conductive film (ES-PACER 300Z, Resonac) on top of the photoresist before performing electron-beam lithography to generate the desired patterns. We then utilize atomic layer deposition to deposit  $\text{TiO}_2$  films with a height at least half the maximum width of the meta-atoms, thereby preventing void formation. The thickness and refractive index of the  $\text{TiO}_2$  films are confirmed by ellipsometry to ensure they match the design specifications. Finally, we apply a high-density plasma reactive ion etching system to remove the excess  $\text{TiO}_2$  on top of the photoresists and then soak the samples in Remover PG to strip away the remaining photoresist.

Using this process, we fabricated two distinct types of holograms tailored to different polarization states, as shown in Figure 2c–f. In Figure 2c,e, each pixel of the Janus metasurface hologram consists of a  $2 \times 2$  array of rectangular meta-atoms arranged in a square lattice. Figure 2d,f reveals vertical side walls and a height of  $613 \text{ nm}$ , closely matching our design targets.

Notably, the scanning electron microscope (SEM) images of the Janus metasurface hologram designed for elliptical polarization (Sample 2, Figure 2e) reveal a noticeable global rotation angle in the top view. This global rotation is a deliberate outcome of the additional rotation angle  $\beta$  applied to the global matrix, which is around  $-24.55^\circ$ .

### 2.3. Optical Characteristics

To predict and verify the reconstructed holographic images of our Janus metasurface holograms, we numerically generated the phase distribution of these images for distinct polarizations and directions through CGH, and imported them into far-field

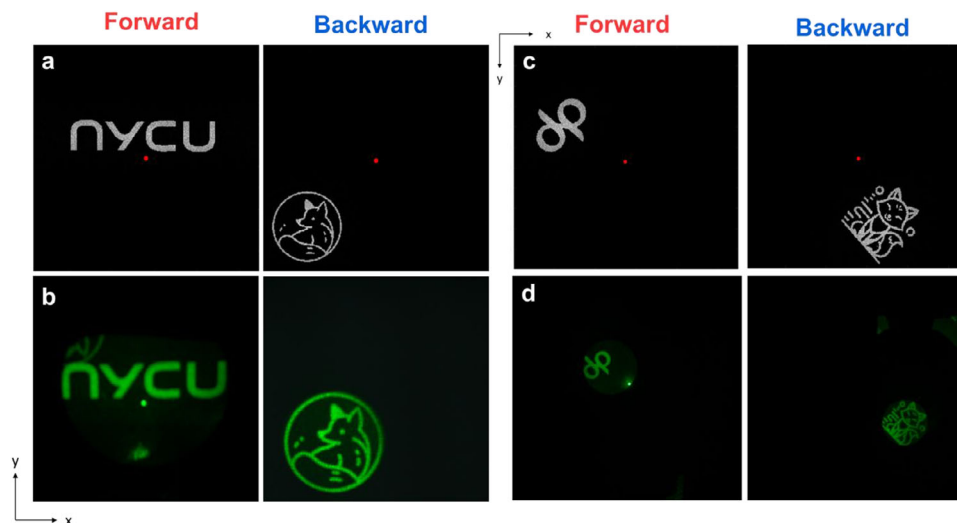


**Figure 4.** Holographic imaging results from Janus metasurface holograms. a,b) The simulated (a) and measured (b) reconstructed images of Sample 1. c,d) The simulated (c) and measured (d) reconstructed images of Sample 2.

diffraction analysis (i.e., fast Fourier transform). The simulated results are presented in **Figure 4a,c**.

In the optical measurements, we constructed an experimental setup to demonstrate the holographic imaging performance of our Janus metasurface holograms (details provided in **Figure S3**, Supporting Information). A single-mode laser with a wavelength of 532 nm was configured as the incident light. Both the polarizer and analyzer consisted of a linear polarizer and a quarter wave-plate. The polarizer was utilized to manipulate the incident polarization states, while the analyzer was employed to analyze the output polarizations. The measured results are shown in **Figure 4b,d**. We evaluated the horizontal FOV of the reconstructed “nycu” image in **Figure 4b** to be  $\approx 20.84^\circ$ , which is in close agreement with the theoretical prediction of  $19.85^\circ$  (details provided in **Figure S2**, Supporting Information).

Compare the simulated and measured holographic images illuminated by our Janus metasurface holograms, red spots at the center in simulations are labeled to describe the zero-order diffraction which corresponds to the bright green spots observed at the center of the measured images. Overall, the experimental results closely match the simulations, exhibiting high imaging quality with no noticeable speckle. This improvement in fidelity is attributed to the incorporation of the Dammann grating, which effectively enhances the image contrast and uniformity.

It is worth noting that the images appear cropped because the analyzer’s aperture—combined with the inherent diffraction angles of the holographic images—limits the region from which light can be collected and imaged. In addition, a relatively weaker image from the backward channel appears under forward incidence when the incident power is increased (**Figure 4b**), which is attributed to minor fabrication imperfections (e.g., deviations in feature widths or occasional missing meta-atoms) and optical misalignments (e.g., slight rotational errors in the linear polarizers, quarter-wave plates, and sample). The high-power images acquired with the analyzer placed at the closest possible distance to the sample are provided in **Figure S4** (Supporting Information).

To evaluate the overall quality of the reconstructed holographic images, we employed two complementary metrics: speckle contrast<sup>[26]</sup> and imaging contrast, each highlighting different aspects of image performance. Speckle contrast is defined as  $C = \sigma/I_b$ , where  $I_b$  and  $\sigma$  are the average and its standard deviation of the image intensity within a selected bright region. This metric quantifies the level of speckle noise; lower  $C$  values correspond to reduced speckle effects, with  $C$  values below 0.3 generally indicating effective speckle suppression. In our measurements, the speckle contrast for the bright region of the “nycu” pattern averaged 0.39, confirming that speckle noise is reasonably well controlled (see **Figure S5**, Supporting Information for full data and analysis).

Imaging contrast, by contrast, measures the visibility of the holographic features relative to the background. It is defined as  $(I_b - I_d)/(I_b + I_d)$ , where  $I_d$  is the average intensity of the image within a selected dark region. Higher values indicate better distinguishability of the projected pattern. In our results, the imaging contrast consistently averaged 0.87, demonstrating that the holographic features are clearly distinguishable from the background and that the overall image quality is excellent (see **Figure S5**, Supporting Information for full data and analysis).

In spite of a coordinate difference between Sample 1 and Sample 2—arising from a design consideration that resulted in flipped meta-atoms arrangement in the  $-y$ -direction (**Figure S6**, Supporting Information)—the measured results demonstrate high robustness and closely match the simulated predictions.

### 3. Discussion and Conclusion

We have successfully demonstrated directionally asymmetric holographic imaging using single-layer  $\text{TiO}_2$ -based Janus metasurface holograms in the visible range. By theoretically analyzing the local and global Jones matrices and applying a global rotation to the sample, our design principle overcomes the limitations of spatial multiplexing and vertical staking, offering greater flexibility for arbitrary incident polarization.

We further integrate Dammann grating theory into our hologram design and employ a configuration of four identical meta-atoms per pixel. The strategy yields high-fidelity holographic images with noticeably reduced speckle noise across an observable FOV. Moreover, the close alignment between the theoretical design and experimental measurements confirms the reliability and accuracy of our approach. Although the measured images appear flipped in the coordinate space, the overall imaging quality and fidelity remain exceptional.

These demonstrated capabilities extend beyond conventional holography applications. Our Janus metasurface design principle is not only applicable to holographic imaging, as shown in this work, but also been validated for orbital angular momentum generation in earlier studies, underscoring its broad potential. Moreover, incorporating tunable, nonlocal materials,<sup>[27]</sup> or matrix Fourier optics<sup>[28]</sup> may further expand the functionalities of these Janus metasurfaces, enabling more dynamic, nonreciprocal optical properties, or multipole polarization control. We anticipate that this versatile platform will drive further innovations across various optical technologies, particularly in scenarios demanding directionally asymmetric light control, such as optical combiners for augmented reality,<sup>[29]</sup> transceivers and receivers for depth sensing,<sup>[30–32]</sup> and cavity-mode modulation in laser systems.<sup>[33]</sup>

## Supporting Information

Supporting Information is available from the Wiley Online Library or from the author.

## Acknowledgements

This work was supported by the National Science and Technology Council in Taiwan (Grant Nos. 113-2112-M-A49-025 and 114-2112-M-A49-007). The authors also acknowledge support from the Ministry of Education in Taiwan under the Yushan Young Scholar Program. This work was performed in part at the Nano Facility Center (NFC) in NYCU, Center for Nano Science and Technology (CNST) in NYCU, and the Taiwan Semiconductor Research Institute (TSRI).

## Conflict of Interest

The authors declare no conflict of interest.

## Author Contributions

Y.-W.H. initiated the study and contributed required materials and analysis tools. C.-Y.L. and Y.-C.C. performed the numerical calculation and simulation. C.-Y.L., Y.-C.C., H.-T.S., Y.-C.W., and C.-Y.H. fabricated metasurface samples. C.-Y.L. and S.-M.C. performed the optical experiments. Y.-C.C., C.-Y.L., and Y.-W.H. analyzed experimental data. Y.-C.C. and Y.-W.H. wrote the manuscript. All authors discussed the results and commented on the manuscript.

## Data Availability Statement

The data that support the findings of this study are available in the supplementary material of this article.

## Keywords

arbitrary polarization, directional asymmetry, holography, Janus metasurfaces, single layer, visible spectrum

Received: May 15, 2025

Revised: August 10, 2025

Published online: September 17, 2025

- [1] J.-Y. Sui, S.-Y. Liao, J.-H. Zou, Q. Chen, Z. Tang, X. Li, C. Yang, C.-M. Guo, Y.-R. Wu, R.-Y. Dong, J. Xu, H.-F. Zhang, *Results Phys.* **2024**, *61*, 107795.
- [2] Z. Zhang, J. E. Raymond, J. Lahann, A. Pena-Francesch, *Adv. Mater.* **2024**, *36*, 2406149.
- [3] R. Zhang, C. Liu, N. Li, L. Chen, T. Xu, Y. Qin, S. Zhang, Z. Wang, *Ind. Eng. Chem. Res.* **2020**, *59*, 18520.
- [4] L. Shang, F. Shangguan, Y. Cheng, J. Lu, Z. Xie, Y. Zhao, Z. Gu, *Nanoscale* **2013**, *5*, 9553.
- [5] Y. Chen, Z. Lou, Z. Chen, S. Yang, J. Hu, J. Wei, *Langmuir* **2022**, *38*, 14387.
- [6] Y. Chen, Z. Chen, J. Wei, *ACS Appl. Nano Mater.* **2023**, *6*, 14702.
- [7] E. Timurdogan, C. V. Poulton, M. J. Byrd, M. R. Watts, *Nat. Photonics* **2017**, *11*, 200.
- [8] L. Feng, M. Ayache, J. Huang, Y.-L. Xu, M.-H. Lu, Y.-F. Chen, Y. Fainman, A. Scherer, *Science* **2011**, *333*, 729.
- [9] E. A. Kittlaus, W. M. Jones, P. T. Rakich, N. T. Otterstrom, R. E. Muller, M. Rais-Zadeh, *Nat. Photonics* **2021**, *15*, 43.
- [10] K. Chen, G. Ding, G. Hu, Z. Jin, J. Zhao, Y. Feng, T. Jiang, A. Alù, C.-W. Qiu, *Adv. Mater.* **2020**, *32*, 1906352.
- [11] Y. Zhou, T. Zhang, G. Wang, Z. Guo, X. Zang, Y. Zhu, F. Ding, S. Zhuang, *Adv. Sci.* **2024**, *11*, 2406571.
- [12] W. Yang, K. Chen, S. Dong, S. Wang, K. Qu, T. Jiang, J. Zhao, Y. Feng, *ACS Appl. Mater. Interfaces* **2023**, *15*, 27380.
- [13] Z. Tang, L. Li, H. Zhang, J. Yang, J. Hu, X. Lu, Y. Hu, S. Qi, K. Liu, M. Tian, J. Jin, Z. Zhang, H. Lin, Y. Huang, *Mater. Des.* **2022**, *223*, 111264.
- [14] J. Ding, N. Xu, H. Ren, Y. Lin, W. Zhang, H. Zhang, *Sci. Rep.* **2016**, *6*, 34020.
- [15] P. Yu, J. Li, S. Zhang, Z. Jin, G. Schütz, C.-W. Qiu, M. Hirscher, N. Liu, *Nano Lett.* **2018**, *18*, 4584.
- [16] Y. Huang, T. Xiao, S. Chen, Z. Xie, J. Zheng, J. Zhu, Y. Su, W. Chen, K. Liu, M. Tang, P. Müller-Buschbaum, L. Li, *Opto-Electron. Adv.* **2023**, *6*, 220073.
- [17] J. Bang, Y. Kim, T. Choi, C. Kim, H. Son, S.-J. Kim, Y. Jeong, B. Lee, *ACS Photonics* **2025**, *12*, 1666.
- [18] Y. Wu, S.-Y. Liao, H.-F. Zhang, *Diam. Relat. Mater.* **2025**, *152*, 111878.
- [19] B. Chen, S. Yang, J. Chen, J. Wu, K. Chen, W. Li, Y. Tan, Z. Wang, H. Qiu, K. Fan, C. Zhang, H. Wang, Y. Feng, Y. He, B. Jin, X. Wu, J. Chen, P. Wu, *Light Sci. Appl.* **2023**, *12*, 136.
- [20] B. Jin, C. Argyropoulos, *Phys. Rev. Appl.* **2020**, *13*, 054056.
- [21] J. Xu, Z. Tang, J.-Y. Sui, H.-F. Zhang, *Opt. Laser Technol.* **2024**, *170*, 110242.
- [22] C.-Y. Lin, J.-H. Huang, H.-T. Su, S.-M. Chang, Y.-C. Wu, Y.-W. Huang, *Adv. Opt. Mater.* **2024**, *12*, 2401335.
- [23] G. Zheng, H. Mühlenbernd, M. Kenney, G. Li, T. Zentgraf, S. Zhang, *Nat. Nanotechnol.* **2015**, *10*, 308.
- [24] Y.-W. Huang, W. T. Chen, W.-Y. Tsai, P. C. Wu, C.-M. Wang, G. Sun, D. P. Tsai, *Nano Lett.* **2015**, *15*, 3122.
- [25] C. Menzel, C. Rockstuhl, F. Lederer, *Phys. Rev. A* **2010**, *82*, 053811.
- [26] J. W. Goodman, *Speckle Phenomena in Optics: Theory and Applications*, 2nd ed., SPIE Press, Bellingham, Washington, **2020**, <https://doi.org/10.1117/3.2548484>.

- [27] H.-T. Su, L.-Y. Wang, C.-Y. Hsu, Y.-C. Wu, C.-Y. Lin, S.-M. Chang, Y.-W. Huang, *Nano Lett.* **2024**, *24*, 10055.
- [28] Y.-T. Liu, Y.-C. Wu, C.-Y. Lin, H.-T. Su, Y.-Q. Zhou, Y.-W. Huang, *Adv. Opt. Mater.* **2025**, *13*, 2500872.
- [29] S. C. Malek, A. C. Overvig, A. Alù, N. Yu, *Light Sci. Appl.* **2022**, *11*, 246.
- [30] X. G. Zhang, Y. L. Sun, B. Zhu, W. X. Jiang, Q. Yu, H. W. Tian, C.-W. Qiu, Z. Zhang, T. J. Cui, *Light Sci. Appl.* **2022**, *11*, 126.
- [31] W.-C. Hsu, C.-H. Chang, Y.-H. Hong, H.-C. Kuo, Y.-W. Huang, *Nano Lett.* **2024**, *24*, 1808.
- [32] W.-C. Hsu, W.-C. Miao, Y.-H. Hong, H.-C. Kuo, Y.-W. Huang, *Nano Lett.* **2025**, *25*, 11382.
- [33] H. Sroor, Y.-W. Huang, B. Sephton, D. Naidoo, A. Vallés, V. Ginis, C.-W. Qiu, A. Ambrosio, F. Capasso, A. Forbes, *Nat. Photon.* **2020**, *14*, 498.